Interlayer Phonon Coupling and Enhanced Electron-Phonon Interactions in Doubly-Aligned hBN/Graphene/hBN Heterostructures

Anish Kumar,[†] Darshit Solanki,[‡] Kenji Watanabe,[¶] Takashi Taniguchi,[¶] A. K. Sood,[*,‡] and Anindya Das[*,‡]

[†]*Undergraduate Programme, Indian Institute of Science, Bangalore, 560012, India*

[‡]*Department of Physics, Indian Institute of Science, Bangalore, 560012, India*

[¶]*National Institute of Material Science, 1-1 Namiki, Tsukuba, 305-0044, Japan*

E-mail: asood@iisc.ac.in; anindya@iisc.ac.in

Abstract

Engineering the band structure via moiré superlattices plays a crucial role in tailoring the electronic and phononic spectra of hBN/graphene heterostructures, enabling a range of emergent properties. While moiré heterostructures have been extensively studied through transport measurements to investigate electronic spectra, their influence on the phononic spectrum, particularly on phonon-phonon and electron-phonon interactions, remains less explored. In this study, we examine the temperature-dependent (8K – 300K) frequency and linewidth responses of the phonon near the K-point of graphene in hBN/graphene/hBN heterostructures for non-aligned, partially aligned, singly aligned, and doubly aligned configurations. The non-aligned samples, where the graphene is rotated by 30° with respect to both top and bottom hBN, exhibit pristine

graphene behavior, characterized by minimal frequency variation with temperature and a typical linewidth increase with increasing temperature. In contrast, doubly aligned samples, where graphene and both hBN are perfectly aligned, display anomalous behavior, with Raman frequency decreasing linearly and the lifetime increasing with increasing temperature. This anomalous anharmonic response could not be explained by the existing models considering only intralayer (within the graphene) phonon-phonon interactions rather indicates the role of strong interlayer phonon-phonon coupling (between hBN and graphene phonons), hitherto not observed. Furthermore, the enhanced electron-phonon interactions due to the resonant condition of phonon decay into electronic channels of doubly aligned hBN/graphene/hBN heterostructures explain the observed linewidth behavior. Our findings demonstrate the ability to engineer phonon-phonon and electron-phonon interactions through alignment of hBN and graphene hexagons, with implications for thermal management and carrier transport optimization in hBN/graphene/hBN heterostructures.

Keywords

Graphene, Raman Spectroscopy, Moiré, Anharmonicity, hBN, Phonons, van der Waals Heterostructures

Introduction

Discovery of hexagonal boron-nitride (hBN) as an atomically smooth and chemically inert substrate for graphene has enabled high-quality devices with exceptional electronic properties, including high mobility and low charge inhomogeneity.[1] Owing to the hexagonal lattice structure of hBN, combined with a bond length comparable to that of graphene, precise alignment of hBN with graphene produces a moiré superlattice structure.[2,3] The moiré superlattice produces a spatially varying potential known as moiré potential, which signifi-

cantly alters the electronic and vibrational properties of graphene. Moiré introduces a large wavelength periodicity (λ_m) in graphene compared to the original unit cell and leads to the emergence of widely reported secondary and tertiary Dirac points.[4,5] Additionally, the moiré superlattice has led to a multitude of recently observed exotic phenomena such as Brown-Zak oscillation, Hofstadter butterfly, electronic ratchet effect, etc.[6–16]

Moiré formation due to the graphene-hBN interface has been extensively studied in the past few years.[9,11,13,17] Despite extensive studies into the formation and electronic correlation effects due to moiré patterns at the graphene-hBN interface, there remains a significant gap in understanding how moiré superlattice affects phonon-phonon and electron-phonon interactions. Understanding phonon dynamics is crucial for understanding the thermal and transport properties of graphene. In graphene-hBN systems, moiré superlattice strongly modulates the phonon spectrum. Reconstruction of the original phonon bands due to band folding and strong hybridization leads to a combination of dispersive and flat phonon bands.[18] Moreover, the interaction of phonon modes in encapsulating hBN layers with those of graphene has so far been overlooked. These phonon modes can significantly influence the system, particularly when they are well-coupled and nearly degenerate with the phonon modes in graphene.

Furthermore, spectroscopic studies of graphene are frequently influenced by the substrate or stress distributions in the case of suspended graphene[19,20], which can obscure the investigation of its intrinsic properties. Substrates such as SiO_2 exhibit high defect densities and charge inhomogeneities, along with substantial lattice mismatches.[21–25] Although hBN as a substrate reduces the defect density, it leads to stress distribution in graphene due to lattice constant and angle mismatch.[26,27] Therefore, a significant challenge is to develop a device that provides a platform for stress-free graphene and effectively mitigates substrate effects.

In this article, we attempt to engineer a hBN-graphene-hBN heterostructure with reduced strain and uncover the intrinsic properties of graphene. We further investigate the effect of emergent moiré pattern due to the hBN alignment with graphene on anharmonic

phonon-phonon and electron-phonon interactions. These interactions are the key determinants of the dispersion of phonon frequency and lifetime as a function of temperature. We conduct temperature-dependent (8K - 300K) Raman spectroscopy of the 2D Raman mode of graphene on different hBN-graphene-hBN alignment regimes with a device structure that allows us to study two different alignment configurations (i) hexagons of hBNs are aligned with the hexagons of graphene - 0° , and (ii) they are rotated by 30° , on a single device. The 30° alignment case - maximally misaligned hBN and graphene - shows the pristine nature of graphene with Raman frequency remaining almost constant with increasing temperature. In contrast, the 0° alignment case - maximally aligned hBN and graphene - exhibits linear decay of Raman frequency by more than 4 cm^{-1} with temperatures from 8K to 300K. We employ different anharmonic models like Klemens model,[28] where the phonon decays into half of its frequency, and other models,[29] where the phonons decay into different combinations of optical and acoustic branches, to explain our data. However, these models remain inadequate to capture the observed trend. Further, an anomalous lifetime increment of K-phonon with increasing temperature for 0° alignment case is observed in contrast to the 30° alignment case with an opposite trend. Our study provides insights into the effect of moiré potential on electron-phonon and phonon-phonon interactions in hBN/graphene/hBN heterostructures, with potential applications in engineering thermal and transport properties of moiré materials.

Results

Fig 1(a,b) shows the schematic of a typical hBN/Gr/hBN heterostructure. By varying the angles between its individual layers, each potentially hosting unique and exotic physics. We focus on the extreme angles between graphene and capping hBNs, specifically at 0° and 30° , with the top and bottom hBN ($\sim$ 30 nm thick) being aligned at 0° / 60° with respect to each other. A monolayer graphene is torn in two parts using the tear-and-stack technique[30,31] and

aligned to top-hBN at 0° (G_0) and 30° (G_{30}) orientations. The top and bottom encapsulation hBN flakes are sourced from a naturally cracked hBN, ensuring easy and precise alignment of the top and bottom hBN at 0° / 60° . Additionally, we fabricate a singly-aligned device, where the top hBN is aligned to the graphene, and the angle between the graphene and the bottom hBN deviates significantly from both 0° and 30° . We also include a standard device, where the angle between any two layers is not close to 0° or 30° , but within a few degrees, to provide baseline measurements. Moving further, we will refer to Doubly-aligned ($BN_0/G_0/BN_0$), Singly-aligned ($BN_0/G_0/BN_{\theta\neq0}$), 30° non-aligned ($BN_0/G_{30}/BN_0$) and the standard device (partially aligned graphene-hBN with $0° < \theta < 30°$) as DA, SA, NA and PA, respectively. **Fig 1(d)** shows an optical micrograph of one such heterostructure with DA and NA configurations. Our device structure provides an ideal platform to perform a comparative study of the effect of moiré between the upper ($\lambda_m \sim 14$ nm at 0°) and lower ($\lambda_m \sim 0.48$ nm at 30°) limits of the moiré wavelength by embedding both limits in a single device using a single flake of graphene, eliminating potentially confounding variables. The atomic stacking configurations of DA **Fig 1(c-left)** and NA **Fig 1(c-right)** show that the carbon atoms and BN atoms are closest and furthest separated in DA and NA, respectively. Thus, the corresponding coupling between the phonons of hBN and those of graphene at the Brillouin zone K points is expected to be maximum and minimum for DA and NA, respectively.

To verify the alignment of the fabricated devices, we measure the full width at half maximum (FWHM) of the 2D Raman peak, which is directly proportional to the moiré wavelength. This approach has been established as a reliable method for assessing the alignment between graphene and hBN.[11,26,27] However, the method's applicability is limited to heterostructures with $< 2°$ misalignment.[26] Our fabrication technique overcomes this limitation by precisely controlling the rotation between two torn flakes and verifying that one flake is aligned close to 0° , thereby ensuring the alignment of the second flake at a desired larger angle. This method non-invasively verifies the alignment of graphene with top and

bottom hBN. The consistency in temperature across different configurations is verified by the anharmonic shift of the hBN peak in Raman spectra. The anharmonic character of the multilayer hBN is expected to remain unaffected by the twist angle as the moiré effect at the graphene-hBN interface decays with the number of layers moving away from the interface. We observe similar anharmonic softening of the hBN peak across all configurations and samples. For the temperature-dependent anharmonic shift of the hBN peak in all configurations, see Supplementary Figure S3.

Fig 2(a) compares the typical Raman spectra for the different configurations. Three Raman active modes from graphene and encapsulating hBN are observed in the spectra. The 2D mode ($\sim$ 2680 cm^{-1}), originating from graphene, involves two near-K phonons with opposite momenta and is the strongest Raman mode of pristine graphene due to the Double Resonance mechanism.[32–34] The near-K phonon involved in the 2D Raman mode corresponds to one of the two phonons (D_1 and D_2) that contribute to the defect-assisted D Raman mode in graphene,[35] which is expected to be at $\sim$ 1350 cm^{-1}. The D mode corresponds to the breathing mode of graphene as shown in **Fig 2(a) (top inset)**. We note that the apparent D mode frequency, $\omega_D = (\omega_{D1} + \omega_{D2})/2$, does not strictly correspond to half the 2D mode frequency. This discrepancy arises due to the double-resonance process of 2D Raman, which involves only the D_1 phonon in Stokes Raman scattering. We will define $\omega_0 \equiv \omega_{2D}/2$, the phonons involved in 2D Raman process, and $\omega_{2D} = 2\omega_0 \neq 2\omega_D$. The G ($\sim$ 1580 cm^{-1}) and hBN ($\sim$ 1370 cm^{-1}) modes, shown in **Fig 2(a) (top inset)**, correspond to the opposite-phase oscillation (E_{2g}) of the two atoms in a unit cell in graphene and hBN, respectively. In our spectrum, the G mode can hardly be seen. This very high-intensity ratio of 2D and G modes establishes the high quality of the devices, being intrinsic or completely undoped.[36] Further, the weak D mode ($\sim$ 1350 cm^{-1}) of graphene establishes the quality of the device. We also observe an anomalous peak ($\omega \sim$1525 cm^{-1}) in **Fig 2(a)**. The frequency of this mode approximately satisfies the Lyddane–Sachs–Teller relation[37] corresponding to the LO counterpart of a TO mode in hBN. This peak is also observed outside the graphene-

heterostructure region, confirming it does not originate from graphene.

The 2D peaks of DA and SA configurations are significantly broadened compared to NA and PA heterostructures, as expected.[11,27] **Fig 2(b)** shows the FWHM of the 2D peak of multiple devices with varying alignments at room temperature. All sections with large angles between graphene and hBN (PA and NA) exhibit 2D peak FWHM of approximately 18 cm^{-1}. The sharpness of the 2D peak confirms the pristine quality of graphene. For graphene aligned to 0° with only one hBN (SA), the 2D peak FWHM increases to approximately 35 cm^{-1}, additional broadening by approximately 17 cm^{-1}. This jump in FWHM has been previously attributed to lattice relaxation and strain distribution due to moiré.[26] We observe a further broadening of the 2D peak to around 56 cm^{-1} when graphene is aligned at 0° to both the top and bottom hBN (DA), consistent with previous studies.[11] The increase in the 2D peak FWHM from non-aligned to single-aligned to double-aligned confirms the symmetric coupling of graphene with top and bottom hBN layers.

Temperature-dependent frequency and linewidth

The measured Raman spectra of 2D mode in the temperature range of 8K to 300K are presented in **Fig 2(c,d)** for NA and DA configurations, respectively. The measured (scatter) data points are overlayed with the fitted voigt function to extract temperature-dependent frequency and linewidth. The dotted straight lines are a guide for the eye to observe changes in spectra with temperature.

The temperature-dependent shift in phonon frequency is primarily influenced by phonon-phonon interactions and lattice thermal expansion. The latter's effect on phonon frequencies is determined by the sign of the Grüneisen parameter, which is positive for in-plane modes of graphene. This positive Grüneisen parameter results in phonon hardening. At lower temperatures, the thermal expansion of graphene, predominantly occurring along the out-of-plane axis, has a negligible effect on in-plane phonon modes. Consequently, this results in a minimal contribution to changes in phonon frequency when compared to the more significant

softening effects caused by anharmonic interactions.[29,38] The phonon-phonon interactions can be approximated to the anharmonic 3-phonon and 4-phonon scatterings and to 3-phonon scattering alone at lower temperatures. We model this frequency shift (Eq. (1)) where the optical phonon decays into two phonons (3-phonon scattering) and extend this model to incorporate multiple decay channels.

$$\omega(T) = \omega_0 + \sum_{\alpha} \chi_\alpha \left(1 + n_B(\omega_1, T) + n_B(\omega_2, T)\right)) \tag{1}$$

where χ_α is the contribution of α^{th} decay channel to 3-phonon scattering and a fitting parameter, $n_B(\omega, T)$ is the Bose occupation factor of phonon with frequency ω at temperature T and $\omega_1 + \omega_2 = \omega_0$, with ω_0 being the phonon frequency in harmonic approximation. The values of ω_1 and ω_2 depend on the decay channels as explained below. The Klemens model, with $\omega_1 = \omega_2 = \omega_0/2$, is widely used[28] for modelling anharmonic shift for many materials without clear justification. We find clear evidence that the Klemens model cannot model the anharmonic character of graphene, and the decay channel must be configured appropriately. Furthermore, we note that a recent report has found that the electron-phonon coupling (EPC) contributes negligibly to anharmonicity in undoped graphene below room temperature.[39] Therefore, we ignore the contributions from electron-phonon coupling mediated frequency shift in our study.

In contrast to the phonon frequency shift, the phonon linewidth depends on both the phonon-phonon and electron-phonon interaction. In a system dominated by phonon-phonon interaction, the linewidth shows a linear trend with a positive slope at higher temperatures. This is because the probability of anharmonic interaction increases with temperature due to elevated phonon population at higher temperatures. As a result, the lifetime of the phonon decreases, and the linewidth broadens. Assuming only 3-phonon interactions (cubic anharmonicity), the change in linewidth of the phonon due to anharmonic interactions (Γ_{ph})

is given by

$$\Gamma^{ph-ph}(T) = \Gamma_0^{ph-ph} + \sum_{\alpha} \Pi_\alpha \left(1 + n_B(\omega_1, T) + n_B(\omega_2, T))\right) \tag{2}$$

where Π_α gives the contribution of the α^{th} decay channel. In an anharmonic system, ω decays into multiple other phonons. In contrast, in a system dominated by electron-phonon coupling, the phonon excites an electron from the valence band to the conduction band, creating an electron-hole pair. An electron-phonon coupled system shows a distinct lifetime temperature dependence compared to an anharmonic system. This behavior is a direct consequence of the fermionic nature of electrons. As the temperature rises, the occupancy of electronic bands increases due to thermal excitation, resulting in a decrease in the number of available empty states for the electron from the valence band to excite. The change in linewidth due to electron-phonon coupling (Γ_{e-ph}) is proportional to the difference in occupation of the initial and final state of the electron (Eq. (3)).[29] The change in energy and momentum of the electron is equal to the phonon energy and momentum. The final expression we use to fit temperature-dependent linewidth data in an electron-phonon dominated system is given by

$$\Gamma^{e-ph}(T) = \Gamma_0^{e-ph} + \gamma \left[n_F(-\omega_0/2, T) - n_F(\omega_0/2, T)\right] \tag{3}$$

where $n_F(\omega, T)$ is the Fermi occupation factor of an electron with energy $\hbar\omega$ at temperature T, ω_0 is the frequency of decaying phonon and γ is the fitting parameters corresponding to the coupling strength.

30° hBN-graphene-hBN

The measured 2D mode frequency ($\omega_{2D} = 2\omega_0$) derives from the temperature dependence of the near-K phonon involved (ω_0). For NA, the temperature dependence of ω_0 is shown in **Fig 3(a)** (see Supplementary Figure 5 for the temperature dependence of G mode in NA configuration). We find that the ω_0 frequency in NA remains temperature-independent in the measured temperature range. We fit the data with Eq. (1) (line in **Fig 3(a)**).

The decay channels and the corresponding weights (χ_α) for ω_0 phonon are obtained from a previous computational study.[29] We will refer to this set of decay channels collectively as the BLM channel. The BLM channel consists of approximately three decay channels with varying weights, as shown in **Fig 4(a)**. We obtain the contribution of the decay channel $\chi_{BLM} \simeq -0.32 \pm 0.43$ cm^{-1}. This vanishing contribution suggests that the real part of the self-energy of the ω_0 phonon in the NA system is negligible in this temperature range. Furthermore, we fit the Klemens model and find a similar vanishing contribution. Note that for a fixed value of χ, the Klemens model predicts the smallest change in frequency. Thus, any 3-phonon channel added to the model can only have a negligible contribution. This shows that the NA system has suppressed anharmonic character. **Fig 3(d)** shows the temperature-dependent FWHM of 2D mode (ω_{2D}). We observe a small broadening of linewidth, suggesting a phonon-phonon interaction dominated system. Accordingly, we fit Eq. (2) with the BLM channel and obtain $\Pi_{BLM} = 4.4 \pm 1.8$ cm^{-1}.

This vanishing frequency shift contrasts sharply with the previous reports of 2D mode frequency shift and linewidth broadening over a similar temperature range.[40–42] Those studies noted a non-linear (slow variation) temperature dependence of phonon frequency at T $\lesssim$ 100K and a linear temperature dependence beyond that. We find a similar non-linear temperature dependence for PA configuration (**Fig 3(b)**), suggesting a sensitive dependence of phonon dynamics on the twist-angle between graphene and hBN. Note that the NA configuration has the smallest possible moiré wavelength and thus will be least influenced by the strain patterns which occur due to domain formation. By reducing the substrate effect of hBN on the encapsulated graphene, our measurements in the NA configuration reveal the intrinsic nature of phonon dynamics in graphene.

Partially aligned hBN-graphene-hBN

Fig 3(b) shows the temperature-dependent frequency of ω_D mode in PA. To evaluate the fitness of these models, we fit temperature-dependent frequency data for PA configuration

with the Klemens model (blue line) and the BLM channel (red line). The BLM channel successfully fits the measurements while the Klemens model deviates significantly. The decay of the D phonon in graphene has been proposed to deviate significantly from the decay channel $\omega_D \rightarrow \omega_D/2 + \omega_D/2$[29] and the inability of the Klemens model to fit the data is as expected. The BLM channel perfectly fits the experimental data with χ_{BLM} = -23.5 ± 0.3 cm^{-1}. This anharmonic coefficient (χ_{BLM}) is nearly 70 times more than that for NA configuration. The only difference between the two configurations is the twist angle. The difference in stress patterns and band folding due to moiré effects, which can enhance the phonon density of states and, therefore, anharmonic character, are some possible reasons behind the amplification of anharmonic character. This observation clearly evidences the fitness of the decay channels predicted in the BLM channel for modelling anharmonic phonon interactions in graphene and the inadequacy of the Klemens model for modelling anharmonic frequency shift in graphene. Furthermore, the linewidth for PA shows a temperature dependence similar to that of NA, with $\Pi_{BLM} \sim 3.36 \pm 0.67$ cm^{-1}, as shown in **Fig 3(e)**. However, we note that the absolute change in the linewidth over the measured temperature range is small ($\sim$ 2 cm^{-1}), and thus, the minute difference in temperature-dependent change between NA and PA, if any, can be obscured.

0° hBN-graphene-hBN

Fig 3(c) shows the temperature-dependent frequency of ω_D mode in DA. In contrast to the NA and PA configurations, the DA configuration with a large moiré wavelength exhibits a distinctly different response to temperature change. Surprisingly, neither the Klemens model nor the BLM channel were found to be adequate for fitting the temperature-dependent frequency shift data. The DA configuration shows a linear temperature dependence throughout the entire measured range, in sharp contrast to the usual non-linear (slow variation) temperature dependence observed in graphene in previous studies[40–42] and our PA configuration. This observed change can originate from the deviation of the decay channel from the previ-

ously calculated BLM decay channel. We will now discuss that this observed linearization can be driven by interlayer phonon coupling between graphene and hBN phonon bands. The frequency of TO mode in hBN at K point ($\omega_{TO} \sim 1300$ cm^{-1}) lies very close to the D phonon frequency in graphene. The Brillouin zone K-points of graphene and encapsulating hBN layers are maximally coupled in the DA configuration. Moreover, the presence of multiple low-energy acoustic phonon bands at the Brillouin zone centre (Γ) of both the graphene and hBN layers can help satisfy the energy conservation during the decay of the near-K ω_0 phonons to hBN near-K phonons. Combining nearly degenerate phonon bands in graphene and hBN at K-point and many low-energy acoustic bands, this channel presents itself as a favourable decay path, as illustrated in **Fig 4(b)**. To verify this claim, we fit the measured data with a single decay channel with variable decay frequency. To this end, we make ω_1 in Eq. (1) a fitting variable. We note a general observation that the low-temperature range linearises as the decay of ω phonon shifts from decaying into $\omega/2$ phonon to phonons of unequal energy. This is expected as the Bose-occupation factor of the lowest energy phonon dictates the temperature dependence at low temperatures. We fit the data with variable ω_1 and find the best fit for $\omega_1 = 1311 \pm 37$ cm^{-1} and the anharmonic coefficient of the hBN channel χ_{BN} = -0.51 $\pm$ 0.73 cm^{-1} (**Fig 3(c)**). The remarkably similar values of ω_1 obtained from fitting and ω_{TO} of hBN at K point strongly suggest the interlayer coupling of phonon bands in graphene and hBN. Since coupling between K-points of the Brillouin zones in graphene and hBN is maximum at 0° / 60° twist-angle and is sensitively dependent on the twist-angle between the two layers, this resonant decay of near-K phonon in graphene to near-K phonon in hBN is only expected to be apparent in DA configuration. The bad fit of the hBN channel for PA configuration, shown with green line **Fig 3(b)**, indicates that the hBN decay channel contribution is vanishing in the PA configuration.

Fig 3(f) shows the temperature-dependent linewidth of 2D mode in DA configuration. The anomalous reduction in linewidth at elevated temperatures suggests that the system is dominated by electron-phonon interactions, as predicted by Eq. (3). It is important to note

that the anharmonic and other interactions do not stop in an electron-phonon dominated system but rather continue in parallel. Thus, it is important to decompose the contributions from multiple mechanisms to the linewidth. Based on previous reports and observations in other configurations, the 2D mode linewidth can be decomposed into three different contributions.

$$\Gamma_{DA}(T) = \Gamma_{intr}(T) + \Gamma_{strain}(T) + \Gamma_{e-ph}(T)$$

The intrinsic linewidth of graphene (Γ_{intr}) contributes to every configuration. Since the NA configuration is closest to an unperturbed graphene, we assert that $\Gamma_{intr}(T) \sim \Gamma_{NA}(T)$. $\Gamma_{intr}(T)$ also captures the linewidth broadening due to the anharmonic decay of phonons. Next, the broadening of $\sim$ 35 cm^{-1} in the DA configuration, over the intrinsic linewidth, with 0° alignment of graphene and hBN, is reported to originate from strain reconstruction within the super-moiré unit cell formed due to a small twist angle between encapsulating hBN layers.[26,27] Due to the robust nature of the lattice reconstruction, we approximate this strain-induced broadening (Γ_{strain}) to be a temperature-independent constant contribution to the total linewidth. Finally, we include the contribution due to electron-phonon interaction (Γ_{e-ph}), which governs the temperature-dependent trend of linewidth. $\Gamma_{e-ph}(T)$ is extracted by subtracting the intrinsic ($\Gamma_{intr}(T)$) and strain (Γ_{strain}) contributions from measured linewidth ($\Gamma_{DA}(T)$) (see Supplementary Figure S4 for extracted $\Gamma_{e-ph}(T)$). The electron-phonon model, Eq. (3), successfully fits the extracted $\Gamma_{e-ph}(T)$ with electron-hole pair creation at frequencies near $\omega_0/2$ and $-\omega_0/2$, respectively. This anomalous electron-phonon coupling in DA configuration is attributed to the moiré induced reconstruction of graphene's electronic band. Flat bands between the high-symmetry M and K points in graphene emerge due to this reconstruction, as illustrated in the dashed rectangular region in **Fig 4(c)**. The energy gap between the flat conduction and valence bands nearly equals the ω_0 phonon energy ($\omega_0 \approx 166$ meV). Thus, the presence of extended flats bands on the Brillouin zone edge of the reconstructed electronic band of graphene enables resonant creation of electron-hole pairs by coupling to near-K phonons, explaining the anomalous electron-

phonon coupling dominated system. We note that previous reports[43,44] of modification in Raman spectra due to resonance between the incident laser energy and the energy separation between the van Hove Singularities of the conduction and valence bands in twisted bilayer graphene around 10-degree twist angle do not apply to our system of hBN/graphene moire, where the van Hove Singularities in the electronic spectrum appear in much lower in energies in PA, SA, DA configurations and far from the laser energy. For NA devices, one can consider almost intrinsic graphene electronic spectrum.

The results have been reproduced in another device for the NA and DA cases, yielding consistent outcomes, as detailed in Supplementary Figure S1. Temperature-dependent behavior of the SA configuration is found to be similar to DA (Supplementary Figure S2), as expected due to the alignment of one of the hBN layers. Furthermore, the temperature dependence of all our configurations shows behaviour distinct from graphene on SiO_2/Si substrate. This has been discussed in details in Supplementary Section S6.

Conclusion

In summary, we have studied the effect of the twist angle between graphene and hBN layers on the 2D Raman mode in graphene using temperature-dependent micro-Raman. A vanishing anharmonicity below 300K in graphene with reduced substrate influence is found. We present evidence of interlayer phonon coupling between phonon modes of graphene and the encapsulating hBN layers in an aligned hBN/graphene/hBN superlattice. We also find an anomalous electron-phonon interaction dominated system in this configuration due to the emergence of flat bands in the graphene superlattice. The study demonstrates the dynamics tunability of phonon dynamics through graphene-hBN twist angle. These results provide an essential understanding of hBN capping effects on phonon in graphene and motivate further studies on the tunability of phonon landscape in graphene and, consequentially, the thermal and transport properties.

Methods

Device Fabrication

Graphene and hexagonal boron nitride flakes were prepared through the standard mechanical exfoliation method using scotch tape, which was then applied to a silicon substrate coated with a 285 nm layer of SiO_2 to enhance the contrast of the graphene flakes. Prior to exfoliation, the substrates were treated with oxygen plasma for 30 seconds to improve the adhesion of the graphene to the substrate. Monolayer graphene was identified through optical contrast and subsequently verified using Raman spectroscopy.

Long, straight edges in graphene and hBN are usually zigzag or armchair edges. For aligning two layers, the zigzag (armchair) edge of the first layer must be aligned with the zigzag (armchair) or the second layer. Thus, the usual practice of aligning straight edges will lead to a theoretical yield limit of 50% for devices with two aligned layers and 25% for devices with three aligned layers, such as in doubly aligned hBN/Gr/hBN devices. To overcome this yield limitation, we use the tear-and-stack technique to pick up a graphene flake at both 0° and 30° angles between apparent straight edges. This ensures that one of the two torn pieces of graphene is aligned with the top hBN at 0° and another at 30°. To ensure alignment of the top and both hBN, we use naturally cracked hBN flakes with straight edges present in both the cracked parts to take into account the misalignment caused by the crack.

All the reported devices are prepared using standard dry transfer technique, utilizing a polydimethylsiloxane(PDMS) hemispherical dome with poly(Bisphenol A carbonate) (PC) film covering the PDMS. This PDMS/PC stamp is prepared on a glass slide and used for the vdW assembly process.

Low-temperature Raman Spectroscopy

Low-temperature Raman spectroscopy is done on HORIBA Scientific Instrument LabRAM HR Evolution attached with a Montana Instruments cryostat, which has the ability to reach

a 4 K base temperature. A laser source with a 532 nm wavelength is used. For spectra collection, a 50× lens with a numerical aperture (NA) of 0.50 was employed. All spectra are recorded with laser power below 1 mW to avoid laser heating. An 1800 lines/mm grating is used in our setup, providing an accuracy of ~ 0.55 cm^{-1}.

Supporting Information

The supporting information is available free of charge at <LINK>.

Additional temperature dependent data for DA configuration, temperature dependent data for the SA configuration, verification of temperature consistency across devices using hBN anharmonicity, extracted electron-phonon interaction induced linewidth change in the DA configuration, data on the temperature dependence of the G mode in the NA configuration, comparison with graphene on a SiO_2/Si substrate, and comparison between the FWHMs of G and 2D peaks.

Acknowledgment

A.K. acknowledges support from the INSPIRE Scholarship for Higher Education (SHE) from the Department of Science and Technology, Government of India as well as from the Center for Emergent Matter Science (CEMS), RIKEN, Japan. A.K.S. thanks the Department of Science and Technology, Government of India for support under the National Science Chair Professorship. A.D. thanks the Department of Science and Technology (DST) and Science and Engineering Research Board (SERB), India, for financial support (SP/SERB-22-0387). A.D. also thanks CEFIPRA project SP/IFCP-22-0005. A.D. and A.K.S. acknowledge the funding support from the Department of Science and Technology (DST/NM/TUE/QM-5/2019), Government of India under the Nanomission. Growing the hBN crystals received support from the Japan Society for the Promotion of Science (KAKENHI grant nos. 19H05790, 20H00354 and 21H05233) to K.W. and T.T.

References

1. Dean, C. R.; Young, A. F.; Meric, I.; Lee, C.; Wang, L.; Sorgenfrei, S.; Watanabe, K.; Taniguchi, T.; Kim, P.; Shepard, K. L.; Hone, J. Boron Nitride Substrates for High-Quality Graphene Electronics. *Nature Nanotech* **2010**, *5*, 722–726.

2. Xue, J.; Sanchez-Yamagishi, J.; Bulmash, D.; Jacquod, P.; Deshpande, A.; Watanabe, K.; Taniguchi, T.; Jarillo-Herrero, P.; LeRoy, B. J. Scanning Tunnelling Microscopy and Spectroscopy of Ultra-Flat Graphene on Hexagonal Boron Nitride. *Nature Mater* **2011**, *10*, 282–285.

3. Decker, R.; Wang, Y.; Brar, V. W.; Regan, W.; Tsai, H.-Z.; Wu, Q.; Gannett, W.; Zettl, A.; Crommie, M. F. Local Electronic Properties of Graphene on a BN Substrate via Scanning Tunneling Microscopy. *Nano Lett.* **2011**, *11*, 2291–2295.

4. Yankowitz, M.; Xue, J.; Cormode, D.; Sanchez-Yamagishi, J. D.; Watanabe, K.; Taniguchi, T.; Jarillo-Herrero, P.; Jacquod, P.; LeRoy, B. J. Emergence of Superlattice Dirac Points in Graphene on Hexagonal Boron Nitride. *Nature Phys* **2012**, *8*, 382–386.

5. Chen, G.; Sui, M.; Wang, D.; Wang, S.; Jung, J.; Moon, P.; Adam, S.; Watanabe, K.; Taniguchi, T.; Zhou, S.; Koshino, M.; Zhang, G.; Zhang, Y. Emergence of Tertiary Dirac Points in Graphene Moiré Superlattices. *Nano Lett.* **2017**, *17*, 3576–3581.

6. Hunt, B.; Sanchez-Yamagishi, J. D.; Young, A. F.; Yankowitz, M.; LeRoy, B. J.; Watanabe, K.; Taniguchi, T.; Moon, P.; Koshino, M.; Jarillo-Herrero, P.; Ashoori, R. C. Massive Dirac Fermions and Hofstadter Butterfly in a van Der Waals Heterostructure. *Science* **2013**, *340*, 1427–1430.

7. Niu, R.; Li, Z.; Han, X.; Qu, Z.; Ding, D.; Wang, Z.; Liu, Q.; Liu, T.; Han, C.; Watanabe, K.; Taniguchi, T.; Wu, M.; Ren, Q.; Wang, X.; Hong, J.; Mao, J.; Han, Z.; Liu, K.; Gan, Z.; Lu, J. Giant Ferroelectric Polarization in a Bilayer Graphene Heterostructure. *Nat Commun* **2022**, *13*, 6241.

8. Zheng, Z.; Ma, Q.; Bi, Z.; de la Barrera, S.; Liu, M.-H.; Mao, N.; Zhang, Y.; Kiper, N.; Watanabe, K.; Taniguchi, T.; Kong, J.; Tisdale, W. A.; Ashoori, R.; Gedik, N.; Fu, L.; Xu, S.-Y.; Jarillo-Herrero, P. Unconventional Ferroelectricity in Moiré Heterostructures. *Nature* **2020**, *588*, 71–76.

9. Makarovsky, O.; Hill, R. J. A.; Cheng, T. S.; Summerfield, A.; Taniguchi, T.; Watanabe, K.; Mellor, C. J.; Patanè, A.; Eaves, L.; Novikov, S. V.; Beton, P. H. High-Temperature Brown-Zak Oscillations in Graphene/hBN Moiré Field Effect Transistor Fabricated Using Molecular Beam Epitaxy. *Commun Mater* **2024**, *5*, 1–6.

10. Ponomarenko, L. A.; Gorbachev, R. V.; Yu, G. L.; Elias, D. C.; Jalil, R.; Patel, A. A.; Mishchenko, A.; Mayorov, A. S.; Woods, C. R.; Wallbank, J. R.; Mucha-Kruczynski, M.; Piot, B. A.; Potemski, M.; Grigorieva, I. V.; Novoselov, K. S.; Guinea, F.; Fal'ko, V. I.; Geim, A. K. Cloning of Dirac Fermions in Graphene Superlattices. *Nature* **2013**, *497*, 594–597.

11. Sun, X.; Zhang, S.; Liu, Z.; Zhu, H.; Huang, J.; Yuan, K.; Wang, Z.; Watanabe, K.; Taniguchi, T.; Li, X.; Zhu, M.; Mao, J.; Yang, T.; Kang, J.; Liu, J.; Ye, Y.; Han, Z. V.; Zhang, Z. Correlated States in Doubly-Aligned hBN/Graphene/hBN Heterostructures. *Nat Commun* **2021**, *12*, 7196.

12. Wang, L.; Gao, Y.; Wen, B.; Han, Z.; Taniguchi, T.; Watanabe, K.; Koshino, M.; Hone, J.; Dean, C. R. Evidence for a Fractional Fractal Quantum Hall Effect in Graphene Superlattices. *Science* **2015**, *350*, 1231–1234.

13. Wang, E.; Lu, X.; Ding, S.; Yao, W.; Yan, M.; Wan, G.; Deng, K.; Wang, S.; Chen, G.; Ma, L.; Jung, J.; Fedorov, A. V.; Zhang, Y.; Zhang, G.; Zhou, S. Gaps Induced by Inversion Symmetry Breaking and Second-Generation Dirac Cones in Graphene/Hexagonal Boron Nitride. *Nature Phys* **2016**, *12*, 1111–1115.

14. Shi, Z.; Jin, C.; Yang, W.; Ju, L.; Horng, J.; Lu, X.; Bechtel, H. A.; Martin, M. C.; Fu, D.;

Wu, J.; Watanabe, K.; Taniguchi, T.; Zhang, Y.; Bai, X.; Wang, E.; Zhang, G.; Wang, F. Gate-Dependent Pseudospin Mixing in Graphene/Boron Nitride Moiré Superlattices. *Nature Phys* **2014**, *10*, 743–747.

15. Dean, C. R.; Wang, L.; Maher, P.; Forsythe, C.; Ghahari, F.; Gao, Y.; Katoch, J.; Ishigami, M.; Moon, P.; Koshino, M.; Taniguchi, T.; Watanabe, K.; Shepard, K. L.; Hone, J.; Kim, P. Hofstadter's Butterfly and the Fractal Quantum Hall Effect in Moiré Superlattices. *Nature* **2013**, *497*, 598–602.

16. Zheng, Z.; Wang, X.; Zhu, Z.; Carr, S.; Devakul, T.; de la Barrera, S.; Paul, N.; Huang, Z.; Gao, A.; Zhang, Y.; Bérubé, D.; Evancho, K. N.; Watanabe, K.; Taniguchi, T.; Fu, L.; Wang, Y.; Xu, S.-Y.; Kaxiras, E.; Jarillo-Herrero, P.; Ma, Q. Electronic Ratchet Effect in a Moiré System: Signatures of Excitonic Ferroelectricity. **2023**, arXiv:2306.03922. arXiv. https://arxiv.org/abs/2306.03922v (accessed April 11, 2025).

17. Wang, L.; Zihlmann, S.; Liu, M.-H.; Makk, P.; Watanabe, K.; Taniguchi, T.; Baumgartner, A.; Schönenberger, C. New Generation of Moiré Superlattices in Doubly Aligned hBN/Graphene/hBN Heterostructures. *Nano Lett.* **2019**, *19*, 2371–2376.

18. Krisna, L. P. A.; Koshino, M. Moiré Phonons in Graphene/Hexagonal Boron Nitride Moiré Superlattice. *Phys. Rev. B* **2023**, *107*, 115301.

19. Huang, C.-W.; Lin, B.-J.; Lin, H.-Y.; Huang, C.-H.; Shih, F.-Y.; Wang, W.-H.; Liu, C.-Y.; Chui, H.-C. Observation of Strain Effect on the Suspended Graphene by Polarized Raman Spectroscopy. *Nanoscale Res Lett* **2012**, *7*, 533.

20. Lin, J.; Guo, L.; Huang, Q.; Jia, Y.; Li, K.; Lai, X.; Chen, X. Anharmonic Phonon Effects in Raman Spectra of Unsupported Vertical Graphene Sheets. *Phys. Rev. B* **2011**, *83*, 125430.

21. Tivanov, M. S.; Kolesov, E. A.; Korolik, O. V.; Saad, A. M.; Komissarov, I. V. Effect of

the Substrate on Phonon Properties of Graphene Estimated by Raman Spectroscopy. *J Low Temp Phys* **2018**, *190*, 20–25.

22. Chen, J.-H.; Jang, C.; Xiao, S.; Ishigami, M.; Fuhrer, M. S. Intrinsic and Extrinsic Performance Limits of Graphene Devices on SiO2. *Nature Nanotech* **2008**, *3*, 206–209.

23. Fratini, S.; Guinea, F. Substrate-Limited Electron Dynamics in Graphene. *Phys. Rev. B* **2008**, *77*, 195415.

24. Zhang, Y.; Brar, V. W.; Girit, C.; Zettl, A.; Crommie, M. F. Origin of Spatial Charge Inhomogeneity in Graphene. *Nature Phys* **2009**, *5*, 722–726.

25. Lee, J.; Lee, N.; Lansac, Y.; Jang, Y. H. Charge Inhomogeneity of Graphene on SiO2: Dispersion-Corrected Density Functional Theory Study on the Effect of Reactive Surface Sites. *RSC Adv.* **2014**, *4*, 37236–37243.

26. Eckmann, A.; Park, J.; Yang, H.; Elias, D.; Mayorov, A. S.; Yu, G.; Jalil, R.; Novoselov, K. S.; Gorbachev, R. V.; Lazzeri, M.; Geim, A. K.; Casiraghi, C. Raman Fingerprint of Aligned Graphene/h-BN Superlattices. *Nano Lett.* **2013**, *13*, 5242–5246.

27. Wang, Z.; Wang, Y. B.; Yin, J.; Tóvári, E.; Yang, Y.; Lin, L.; Holwill, M.; Birkbeck, J.; Perello, D. J.; Xu, S.; Zultak, J.; Gorbachev, R. V.; Kretinin, A. V.; Taniguchi, T.; Watanabe, K.; Morozov, S. V.; Anđelković, M.; Milovanović, S. P.; Covaci, L.; Peeters, F. M. *et al.* Composite Super-Moiré Lattices in Double-Aligned Graphene Heterostructures. *Science Advances* **2019**, *5*, eaay8897.

28. Klemens, P. G. Anharmonic Decay of Optical Phonons. *Phys. Rev.* **1966**, *148*, 845–848.

29. Bonini, N.; Lazzeri, M.; Marzari, N.; Mauri, F. Phonon Anharmonicities in Graphite and Graphene. *Phys. Rev. Lett.* **2007**, *99*, 176802.

30. Kim, K.; Yankowitz, M.; Fallahazad, B.; Kang, S.; Movva, H. C. P.; Huang, S.; Larentis, S.; Corbet, C. M.; Taniguchi, T.; Watanabe, K.; Banerjee, S. K.; LeRoy, B. J.;

Tutuc, E. Van Der Waals Heterostructures with High Accuracy Rotational Alignment. *Nano Lett.* **2016**, *16*, 1989–1995.

31. Hu, J.; Tan, J.; Al Ezzi, M. M.; Chattopadhyay, U.; Gou, J.; Zheng, Y.; Wang, Z.; Chen, J.; Thottathil, R.; Luo, J.; Watanabe, K.; Taniguchi, T.; Wee, A. T. S.; Adam, S.; Ariando, A. Controlled Alignment of Supermoiré Lattice in Double-Aligned Graphene Heterostructures. *Nat Commun* **2023**, *14*, 4142.

32. Saito, R.; Jorio, A.; Souza Filho, A. G.; Dresselhaus, G.; Dresselhaus, M. S.; Pimenta, M. A. Probing Phonon Dispersion Relations of Graphite by Double Resonance Raman Scattering. *Phys. Rev. Lett.* **2001**, *88*, 027401.

33. ying Wang, Y.; hua Ni, Z.; Yu, T.; Shen, Z. X.; min Wang, H.; hong Wu, Y.; Chen, W.; Shen Wee, A. T. Raman Studies of Monolayer Graphene: The Substrate Effect. *J. Phys. Chem. C* **2008**, *112*, 10637–10640.

34. Thomsen, C.; Reich, S. Double Resonant Raman Scattering in Graphite. *Phys. Rev. Lett.* **2000**, *85*, 5214–5217.

35. Cançado, L. G.; Pimenta, M. A.; Saito, R.; Jorio, A.; Ladeira, L. O.; Grueneis, A.; Souza-Filho, A. G.; Dresselhaus, G.; Dresselhaus, M. S. Stokes and Anti-Stokes Double Resonance Raman Scattering in Two-Dimensional Graphite. *Phys. Rev. B* **2002**, *66*, 035415.

36. Casiraghi, C. Doping Dependence of the Raman Peaks Intensity of Graphene Close to the Dirac Point. *Phys. Rev. B* **2009**, *80*, 233407.

37. Lyddane, R. H.; Sachs, R. G.; Teller, E. On the Polar Vibrations of Alkali Halides. *Phys. Rev.* **1941**, *59*, 673–676.

38. Chen, X.; Lin, M. L.; Cong, X.; Leng, Y. C.; Zhang, X.; Tan, P. H. Intrinsic Phonon

Anharmonicity in Heavily Doped Graphene Probed by Raman Spectroscopy. *Carbon* **2021**, *185*, 282–288.

39. Erhardt, N. G.; Castellano, A.; Batista, J. P. A.; Bianco, R.; Lončarić, I.; Verstraete, M. J.; Novko, D. Electron-Mediated Anharmonicity and Its Role in the Raman Spectrum of Graphene. **2024**, arXiv:2410.23791. arXiv. https://arxiv.org/abs/2410.23791 (accessed April 11, 2025).

40. Hosoya, N.; Akaho, Y.; Inoue, M.; Sahoo, S.; Tachibana, M. Temperature Dependence of the Raman Spectra of Polycrystalline Graphene Grown by Chemical Vapor Deposition. *Applied Physics Letters* **2014**, *105*, 023108.

41. Liu, H. N.; Cong, X.; Lin, M. L.; Tan, P. H. The Intrinsic Temperature-Dependent Raman Spectra of Graphite in the Temperature Range from 4K to 1000K. *Carbon* **2019**, *152*, 451–458.

42. Han, Z.; Yang, X.; Sullivan, S. E.; Feng, T.; Shi, L.; Li, W.; Ruan, X. Raman Linewidth Contributions from Four-Phonon and Electron-Phonon Interactions in Graphene. *Phys. Rev. Lett.* **2022**, *128*, 045901.

43. Kim, K.; Coh, S.; Tan, L. Z.; Regan, W.; Yuk, J. M.; Chatterjee, E.; Crommie, M. F.; Cohen, M. L.; Louie, S. G.; Zettl, A. Raman Spectroscopy Study of Rotated Double-Layer Graphene: Misorientation-Angle Dependence of Electronic Structure. *Phys. Rev. Lett.* **2012**, *108*, 246103.

44. Jorio, A.; Cançado, L. G. Raman Spectroscopy of Twisted Bilayer Graphene. *Solid State Communications* **2013**, *175–176*, 3–12.

45. Anđelković, M.; Milovanović, S. P.; Covaci, L.; Peeters, F. M. Double Moiré with a Twist: Supermoiré in Encapsulated Graphene. *Nano Lett.* **2020**, *20*, 979–988.

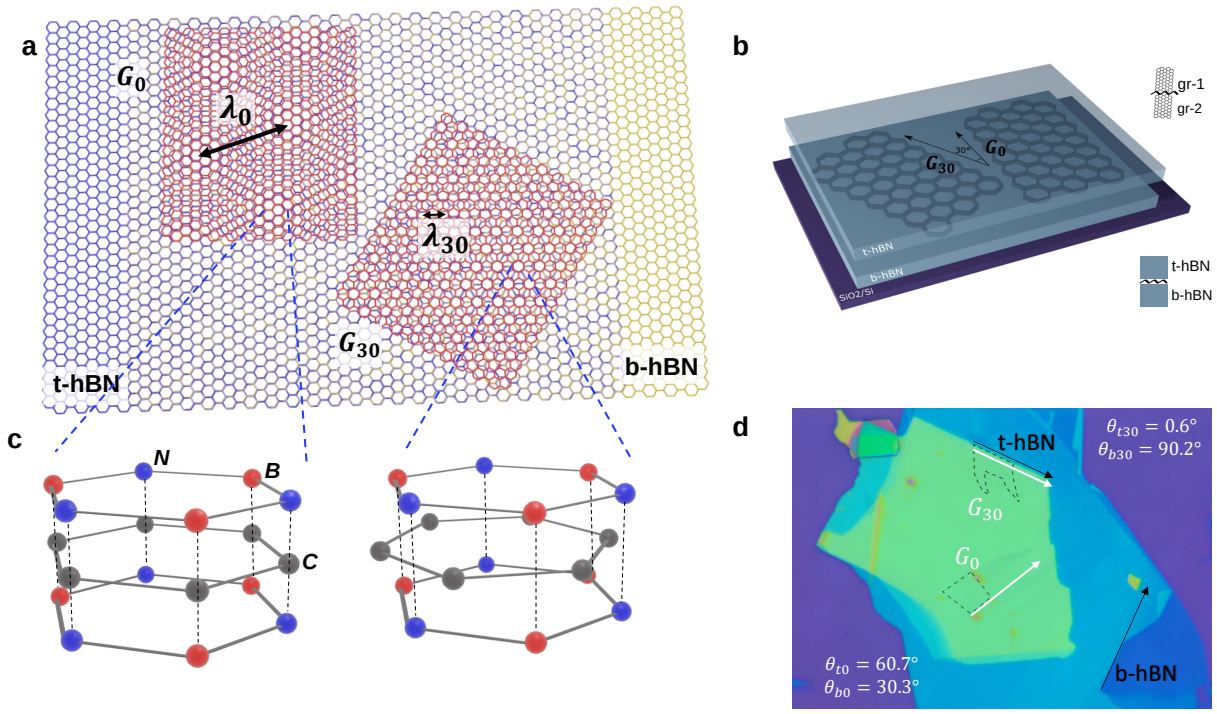

Figure 1: **(a)** Emergence of a long (short) wavelength [λ_0 (λ_{30})] moiré pattern due to a twist angle of 0° (30°) between graphene flake G_0 (G_{30}) and encapsulating hBN layers, labelled as t-hBN and b-hBN. **(b)** Schematic of a typical device. The insets show that the graphene flakes (G_0 and G_{30}) and the hBN flakes (t-hBN and b-hBN) are torn from a common larger graphene and hBN flake, respectively. **(c)** Atomic view of the local stacking in the region pointed by the dashed lines. Local stacking near G_0 graphene shows the boron and nitrogen atoms directly on top of the carbon atoms in graphene. In contrast, the local stacking near G_{30} graphene shows the boron and nitrogen atoms maximally separated from the carbon atoms in graphene. **(d)** An optical image of a device. The white and black arrows show the crystallographic axis of graphene and hBN layers, respectively, assessed by straight edges of the layers. θ_{ij} is the optically estimated twist angle between i-hBN and G_j.

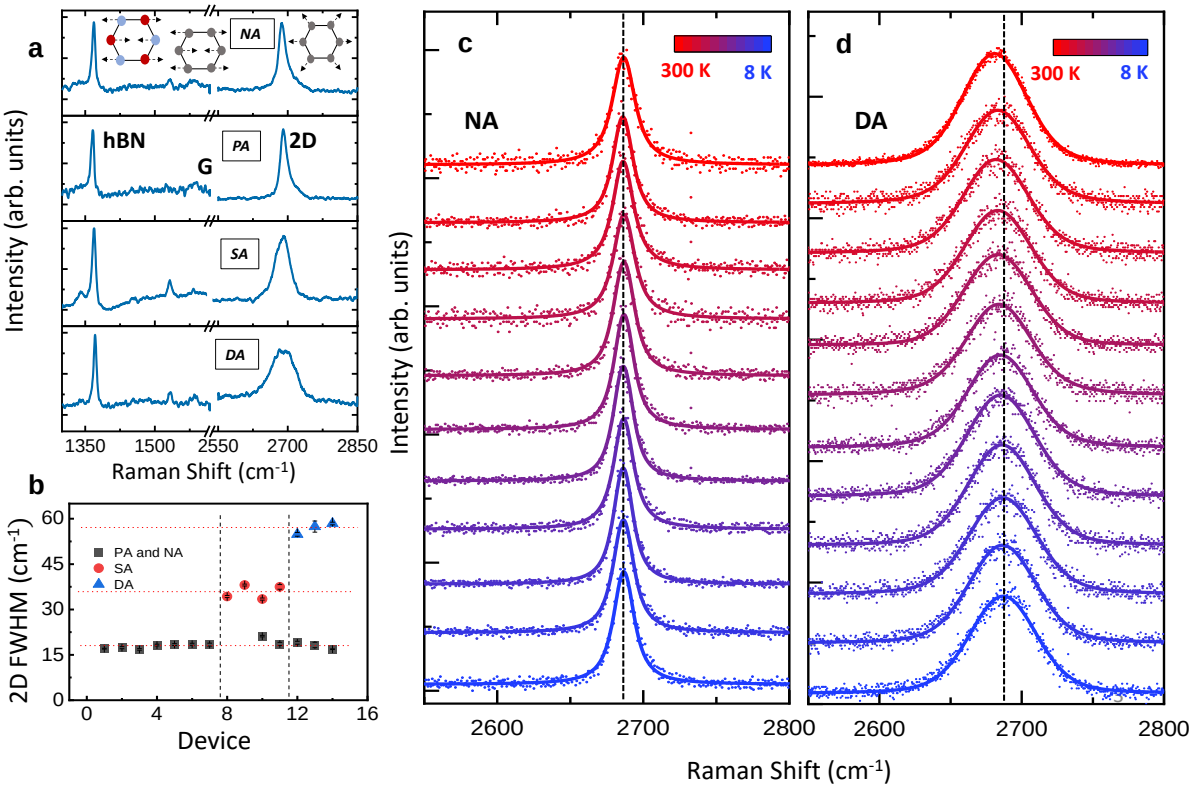

Figure 2: **(a)** In order from top to bottom, the panels show typical room-temperature spectrum for non-aligned (NA), partially-aligned (PA), singly-aligned (SA) and doubly-aligned (DA) configurations. The inset in the top panel illustrates the vibrational mode for (left to right) E_{2g} mode of hBN, G mode of graphene and 2D mode of graphene, as labelled in the second panel. **(b)** Statistics of the linewidth of 2D mode for multiple devices. The vertical dashed line separates the types of devices, and the horizontal line illustrates the discrete jump in linewidth between different configurations. **(c)** Spectra of 2D mode for various temperatures in NA configuration. **(d)** Spectra of 2D mode for various temperatures in DA configuration. The vertical dashed lines in **(c, d)** are a guide to the eye to see the movement of the peak frequency.

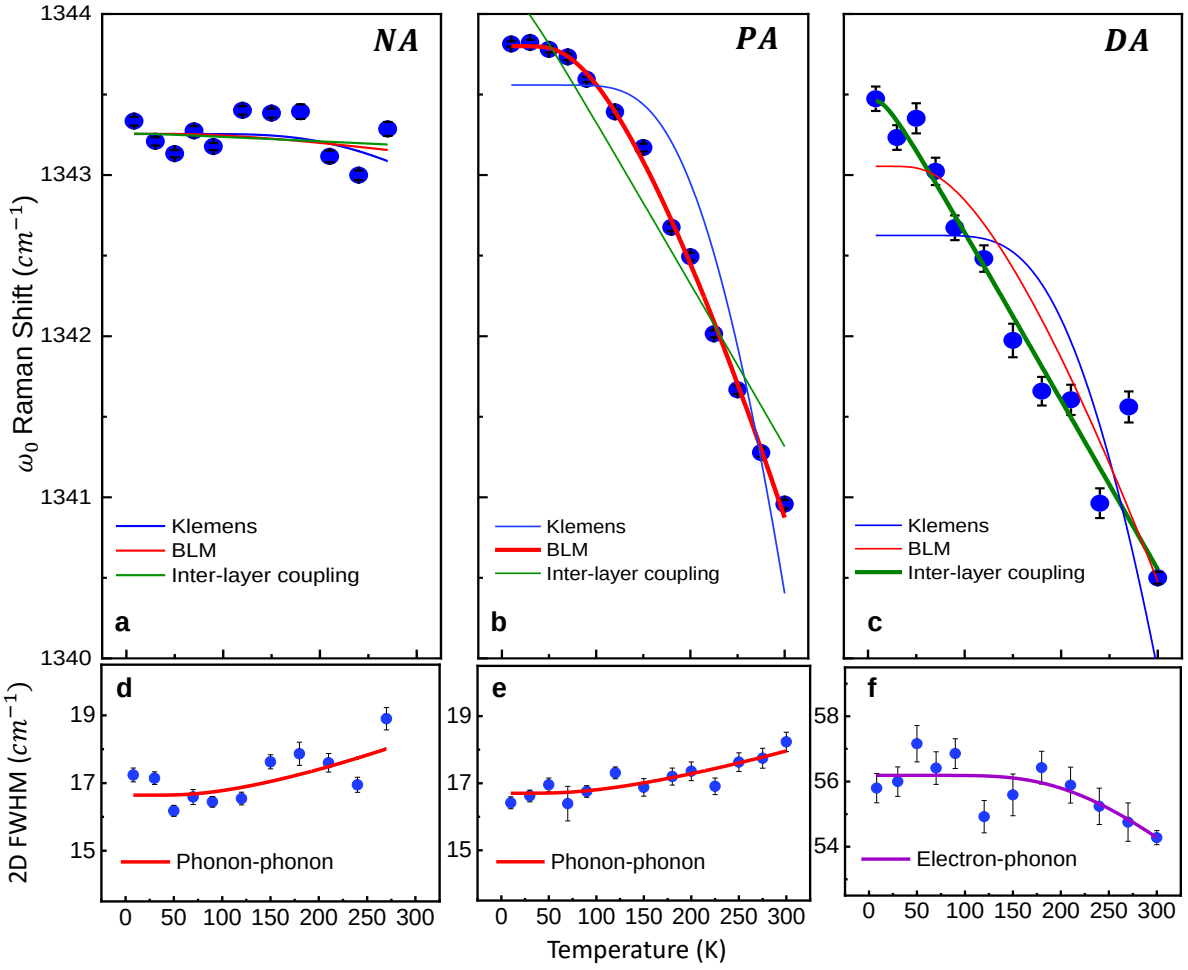

Figure 3: **(a,b,c)** The scatter points show the temperature-dependent frequency change of the phonon ($\omega_0 = \omega_{2D}/2$) involved in 2D Raman process for non-aligned (NA), partially-aligned (PA) and doubly-aligned (DA) configurations, respectively. The blue, red and green solid lines show the best fitting for the Klemens model, BLM model and inter-layer coupling model, respectively. The best fitting model is shown with a thicker line. The fittings for all models overlap in **(a)**. **(d,e,f)** The scatter points show the fitted 2D mode linewidth for varying temperatures. The red lines show the fitting using Eq (2) in **(d,e)** and using Eq (3) in **(f)**.

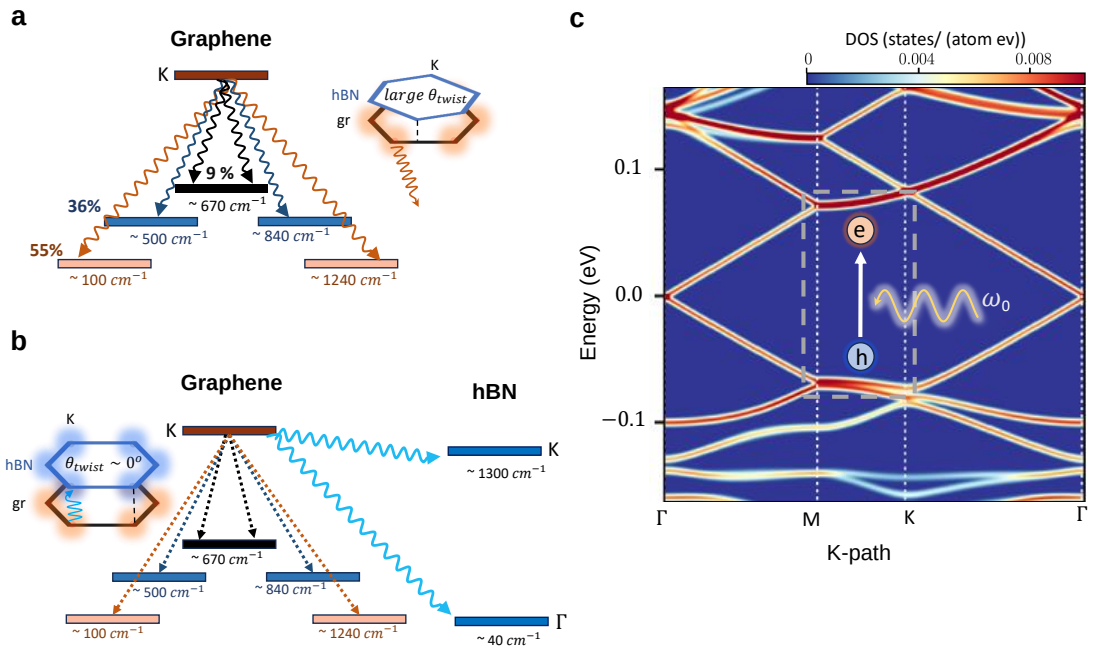

Figure 4: **(a)** Illustration of different decay channels involved in the BLM decay channel. The thickness of the arrow represents the relative strength of the channel. The calculated contribution[29] for each decay channel is mentioned in percentage beside the channel. The approximate phonon mode frequencies are mentioned below the phonon bands (rectangular boxes). The inset shows the Brillouin zone of graphene and hBN, and phonon emission from K point, decaying, without any influence from encapsulating the hBN layer at a large twist angle. **(b)** The dashed lines represent the quenching of the BLM decay channel in the DA configuration. The solid line shows the dominating channel. The inset shows the phonon decaying from the K point of graphene to the K point of hBN when closely aligned. **(c)** The electronic band structure with the density of states (color bar) of DA configuration. The dashed rectangle highlights the region with flat bands, where the band gap is nearly resonant to the phonon energy ($\hbar\omega_0$). Adapted with permission from reference.[45] Copyright 2024 American Chemical Society.

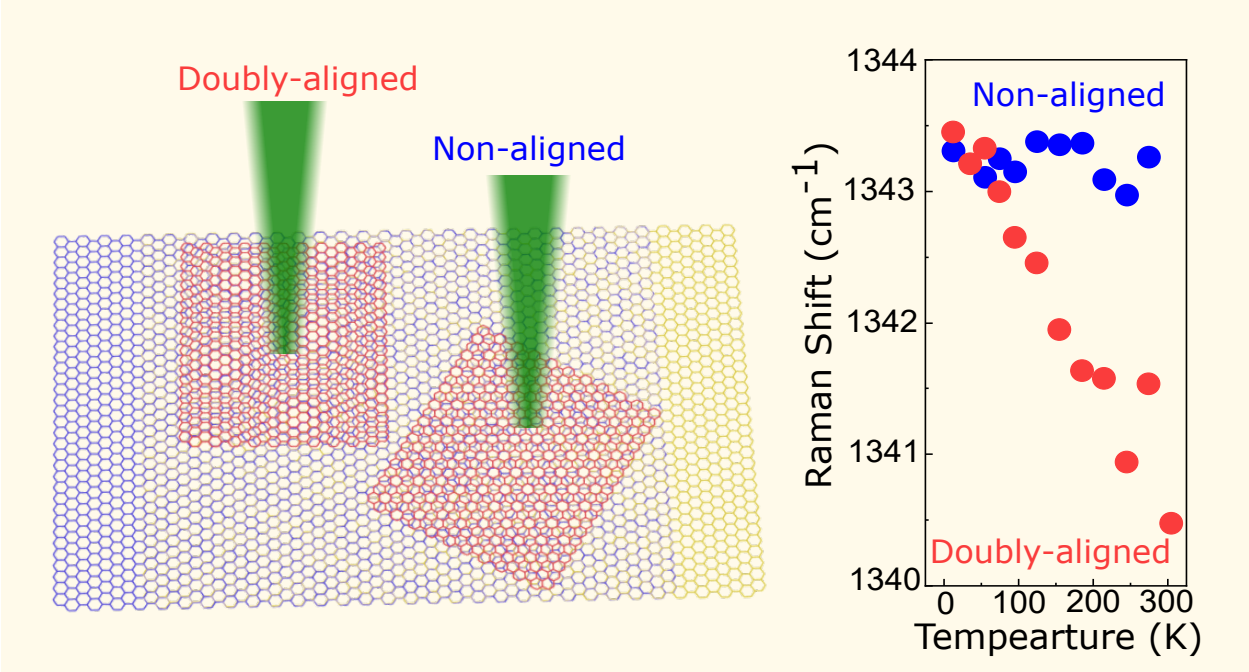

For Table of Contents Only

Supporting Information

Interlayer Phonon Coupling and Enhanced Electron-Phonon Interactions in Doubly-Aligned hBN/Graphene/hBN Heterostructures

Anish Kumar,[†] Darshit Solanki,[‡] Kenji Watanabe,[¶] Takashi Taniguchi,[¶] A. K. Sood,[*,‡] and Anindya Das[*,‡]

[†]*Undergraduate Programme, Indian Institute of Science, Bangalore, 560012, India*

[‡]*Department of Physics, Indian Institute of Science, Bangalore, 560012, India*

[¶]*National Institute of Material Science, 1-1 Namiki, Tsukuba, 305-0044, Japan*

E-mail: asood@iisc.ac.in; anindya@iisc.ac.in

S1. Additional temperature dependence data

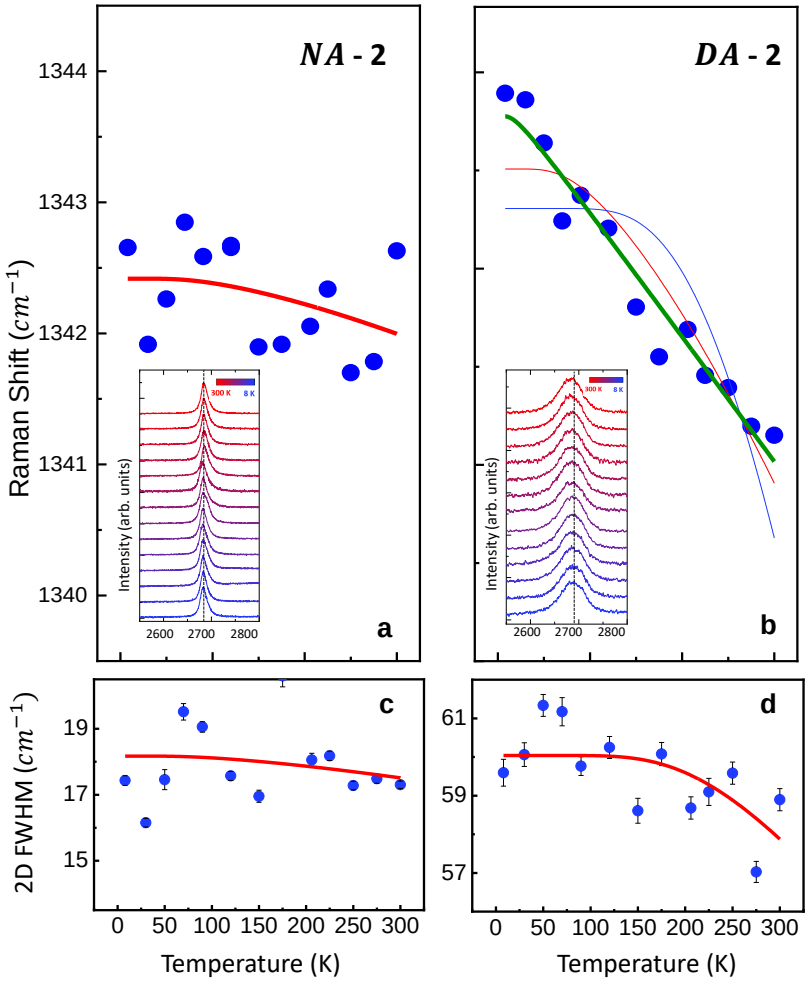

Figure S1: **(a,b)** The scatter points show the evolution of fitted D phonon frequency ($\omega_{2D}/2$) with temperature for NA and DA configurations, respectively, from another device. The blue, red and green solid lines show the best fitting for the Klemens model, BLM model and interlayer coupling model, respectively. The thicker line shows the model with the best fitting. All fits are approximately overlapping in **(a)**. The insets show the stacked spectra with a straight line as a guide to the eye for the corresponding configurations. **(c,d)** The scatter points show the fitted 2D mode linewidth for varying temperatures. The red lines show the fitting using the phonon-phonon BLM model and electron-phonon model (see main text) for (c) and (d), respectively.

S2. Temperature dependence data for SA configuration

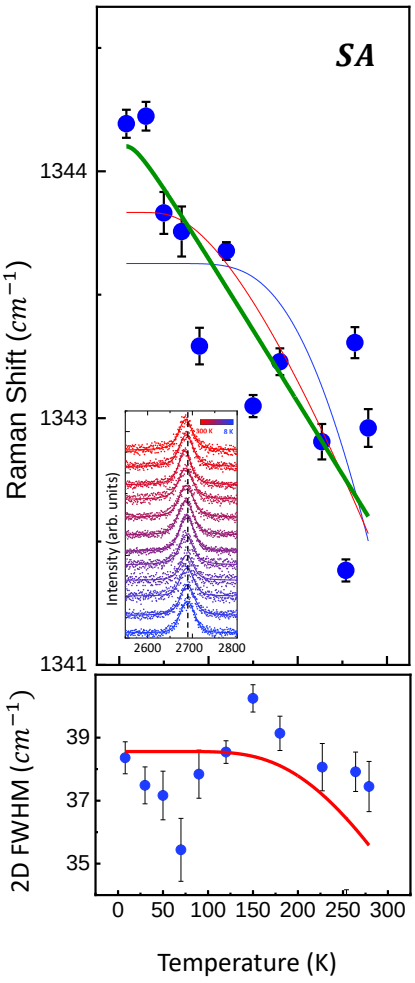

Figure S2: **(top)** The scatter points show the evolution of fitted D phonon frequency ($\omega_{2D}/2$) with temperature for SA configuration. The blue, red and green solid lines show the best fitting for the Klemens model, BLM model and inter-layer coupling model, respectively. The thicker line shows the model with the best fitting. **(bottom)**The scatter points show the fitted 2D mode linewidth for varying temperatures. The red lines show the fitting using the electron-phonon model (see main text). The inset shows the stacked spectra with a straight line as a guide to the eye for the SA configuration.

S3. Verifying temperature consistency across devices using hBN anharmonicity

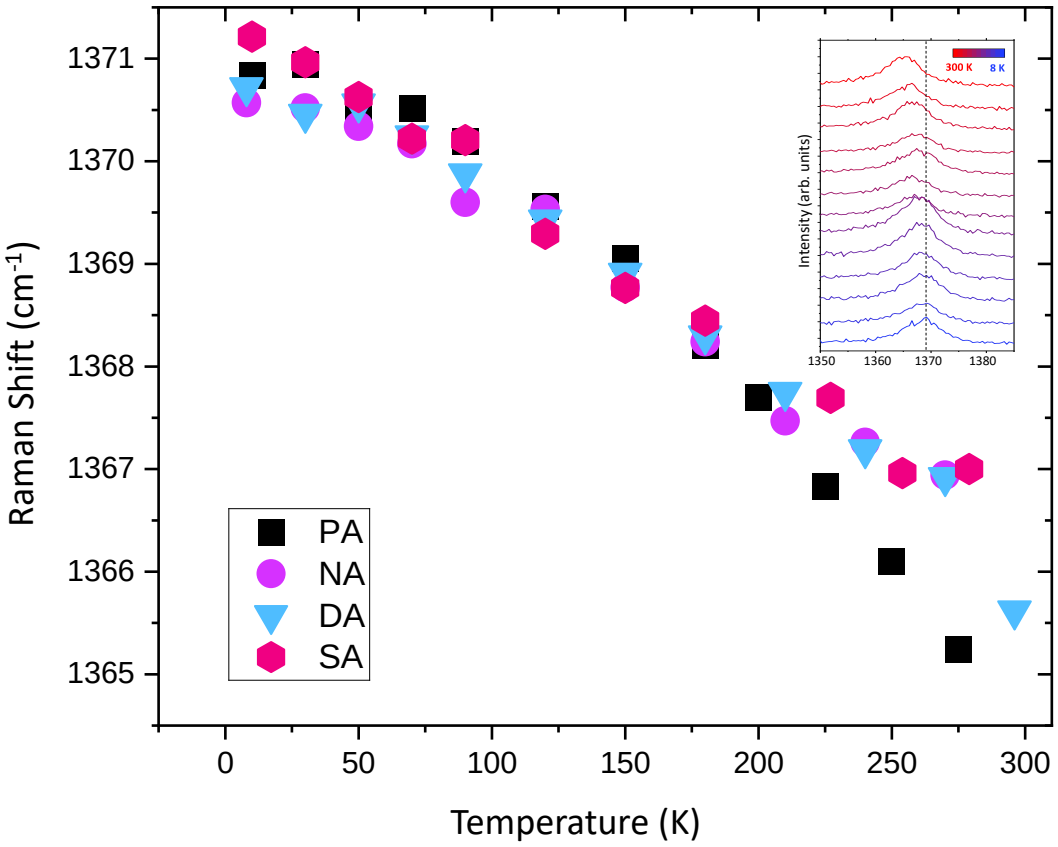

8

Figure S3: Temperature-dependent frequent shift of hBN Raman peak for all the different configurations. Similar values and trends in frequency softening verify the consistency of temperature across all measured devices and configurations. Note that NA and DA are two different configurations on the same device, while PA and SA are from different devices. The inset shows the stacked spectra for hBN Raman mode in DA configuration, which is representative of spectra from all configurations.

S4. Extracted electron-phonon interaction induced linewidth change in DA configuration

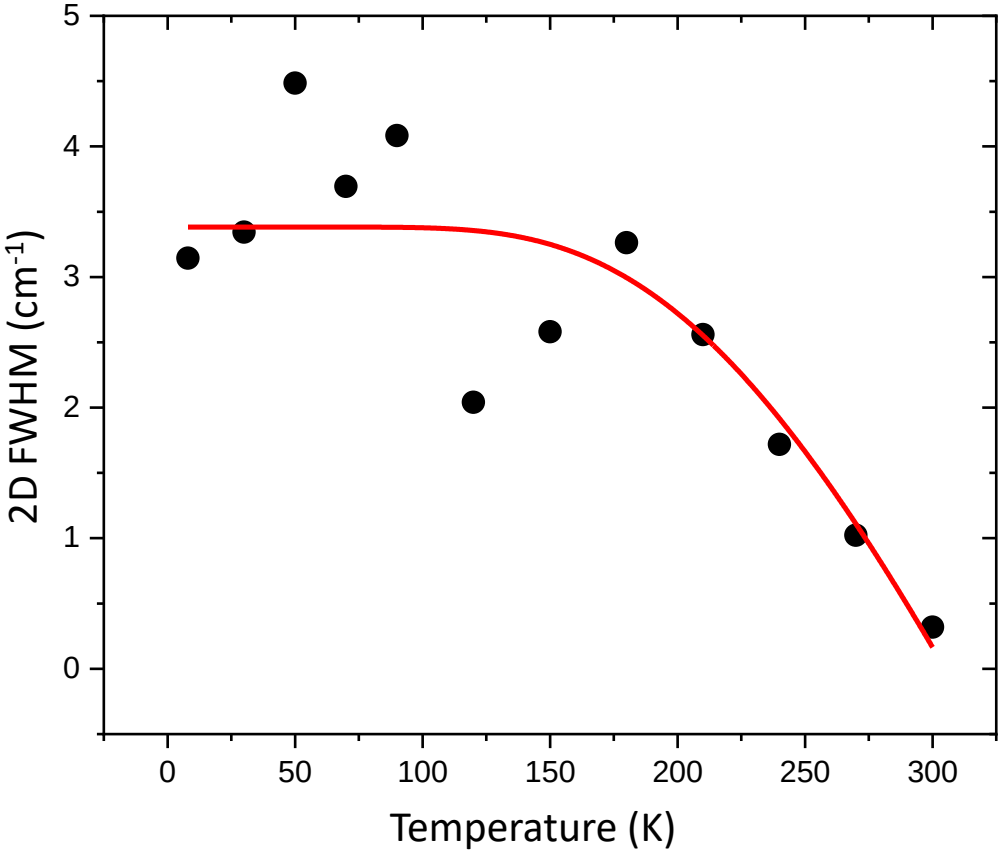

9

Figure S4: The scatter points show the extracted $\Gamma_{e-ph} = \Gamma_{DA}(T) - \Gamma_{intr}(T) - \Gamma_{strain}$ where $\Gamma_{intr}(T) \sim \Gamma_{NA}(T)$ and $\Gamma_{strain} \sim 36$ cm^{-1} based on observed jump in linewidth between NA and DA configuration at low temperature. The red line shows the electron-phonon model fit.

S5. Temperature dependence of G mode in NA configuration

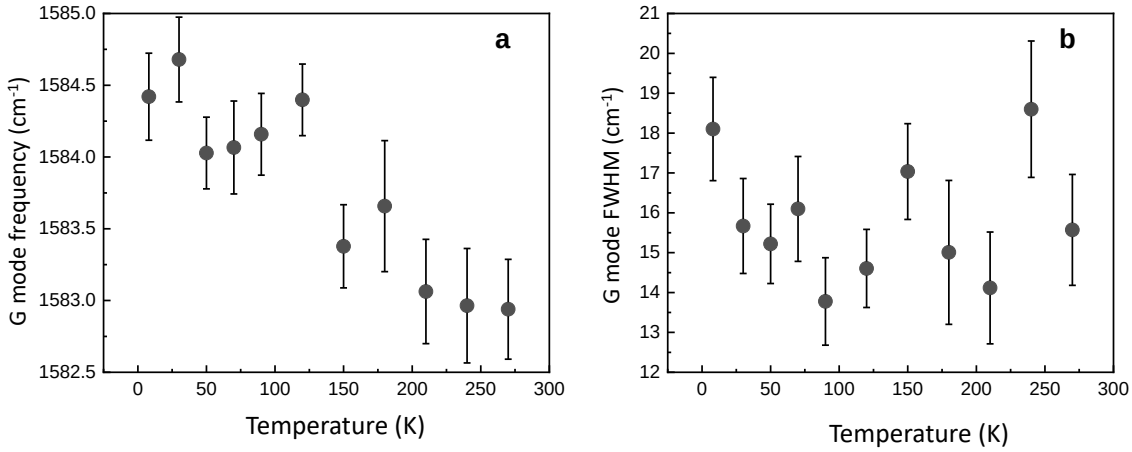

15

Figure S5: The temperature-dependent (a) frequency and (b) linewidth of G mode in NA configuration.

S6. Comparison with Graphene on SiO_2/Si substrate

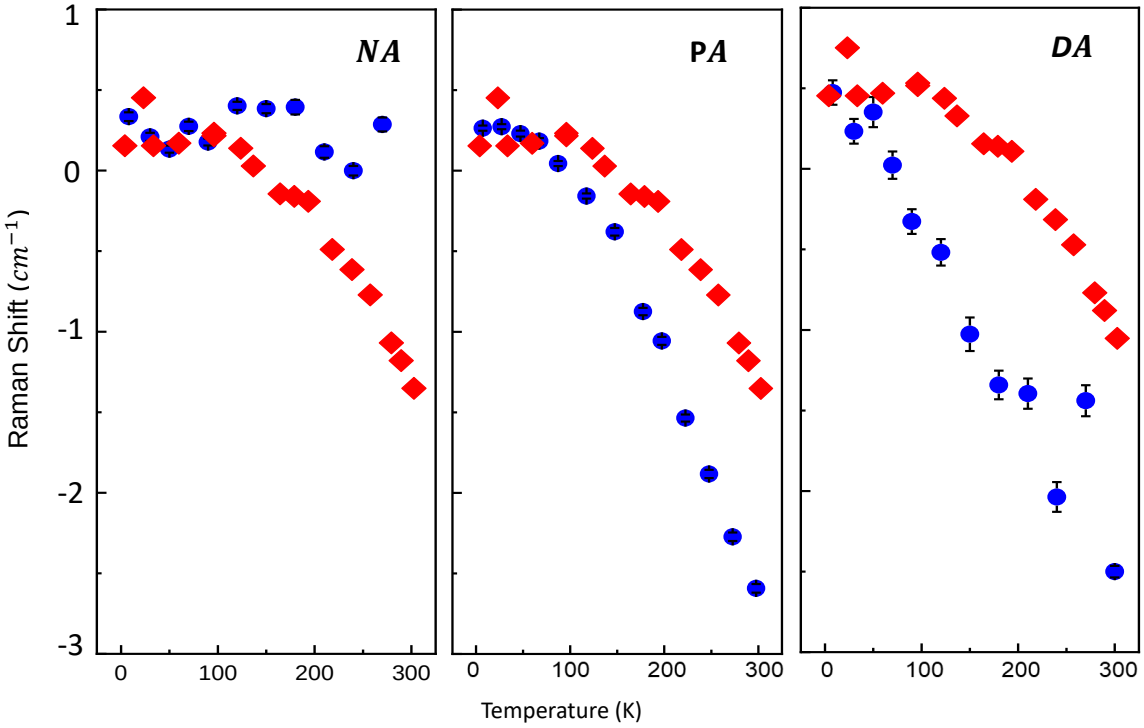

Figure S6: The blue circular scatter points show the temperature-dependent frequency shift of (a) NA (b) PA (c) DA configurations. The red triangle scatter points in each panel show the temperature-dependence frequency shift of 2D mode for graphene on SiO_2/Si from Liu et al.[1]

Figure S6 compares the frequency response of our configurations (NA, PA, and DA) with graphene on SiO_2/Si substrate. For graphene on SiO_2/Si substrate, the frequency shows a non-linear response (within 120 K, almost no change and above it linear decay). It can be seen that among the three configurations, PA resembles close to the SiO_2/Si substrate. On SiO_2/Si substrate, the phonons are affected by the nanometre scale roughness of the SiO_2/Si surface, which is known to produce strain as well as unintentional doping, etc, which affects the anharmonicity. Therefore, graphene on SiO_2/Si substrate is different from our DA configuration. Though both (graphene on SiO_2/Si substrate and DA) have enhanced anharmonicity, their nature of decay with temperature is quite distinct, as evident from Fig S6.

S7. Comparison of 2D and G peak FWHM

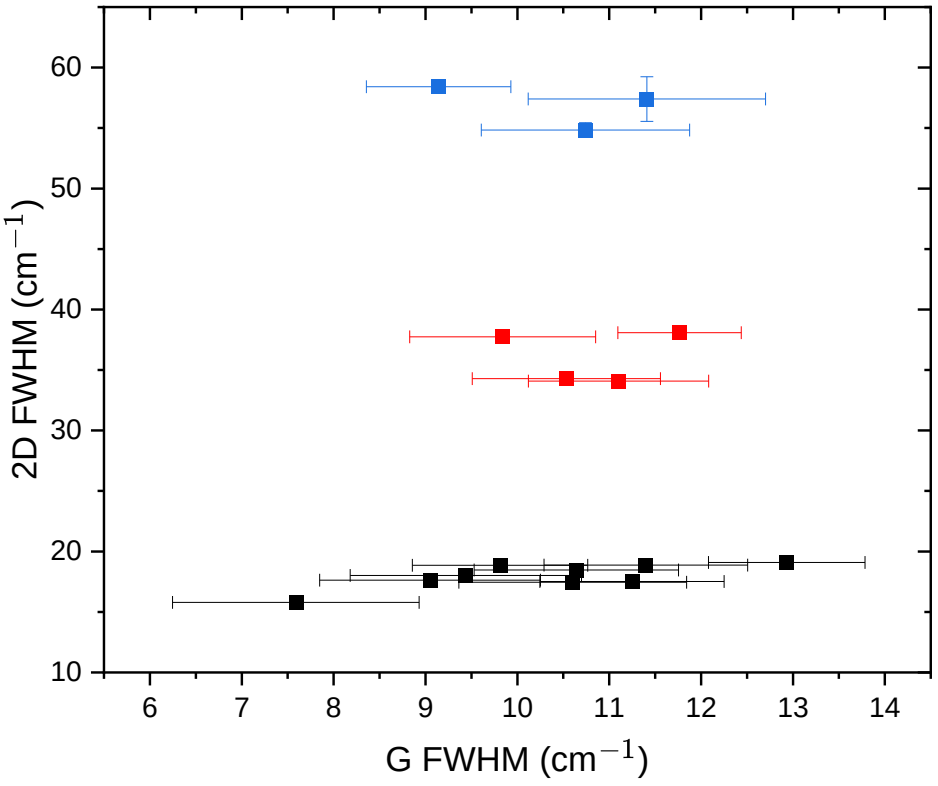

Figure S7: 2D FWHM vs G FWHM for devices shown in Fig 2b of the main text. The black, red and blue squares are for PA/NA, SA and DA samples, respectively. The large error bar in the G-linewidth is due to its very low intensity for our hBN-encapsulated ultra-clean devices.

References

(1) Liu, H. N.; Cong, X.; Lin, M. L.; Tan, P. H. The Intrinsic Temperature-Dependent Raman Spectra of Graphite in the Temperature Range from 4K to 1000K. *Carbon* **2019**, *152*, 451–458.